# Shock-Induced Turbulence and Acoustic Loading on Aerospace Structures

**Dimitris Drikakis**

**CRANFIELD UNIVERSITY**
**CRANFIELD DEFENCE AND SECURITY**
**COLLEGE ROAD**
**BEDFORD MK430AL UNITED KINGDOM**

Report Date: August 2015

Final Report from 1 August 2014 to 31 July 2015

**Air Force Research Laboratory**
**Air Force Office of Scientific Research**
**European Office of Aerospace Research and Development**
**Unit 4515, APO AE 09421-4515**

| REPORT DOCUMENTATION PAGE | | Form Approved OMB No. 0704-0188 |
|---|---|---|

| 1. REPORT DATE *(DD-MM-YYYY)* | 2. REPORT TYPE | 3. DATES COVERED *(From – To)* |
|---|---|---|
| 22 August 2015 | Final Report | 1 August 2014 – 31 July 2015 |

**4. TITLE AND SUBTITLE**

**Shock-Induced Turbulence and Acoustic Loading on Aerospace Structures**

**5a. CONTRACT NUMBER**

**5b. GRANT NUMBER**

**FA9550-14-1-0224**

**5c. PROGRAM ELEMENT NUMBER**

61102F

**6. AUTHOR(S)**

**Dimitris Drikakis**

**5d. PROJECT NUMBER**

**5d. TASK NUMBER**

**5e. WORK UNIT NUMBER**

**7. PERFORMING ORGANIZATION NAME(S) AND ADDRESS(ES)**
CRANFIELD UNIVERSITY
CRANFIELD DEFENCE AND SECURITY
COLLEGE ROAD
BEDFORD MK430AL UNITED KINGDOM

**8. PERFORMING ORGANIZATION REPORT NUMBER**

N/A

**9. SPONSORING/MONITORING AGENCY NAME(S) AND ADDRESS(ES)**

EOARD
Unit 4515
APO AE 09421-4515

**10. SPONSOR/MONITOR'S ACRONYM(S)**

AFRL/AFOSR/IOE (EOARD)

**11. SPONSOR/MONITOR'S REPORT NUMBER(S)**

**AFRL-AFOSR-UK-TR-2015-0041**

**12. DISTRIBUTION/AVAILABILITY STATEMENT**

**Distribution A: Approved for public release; distribution is unlimited.**

**13. SUPPLEMENTARY NOTES**

**14. ABSTRACT**
An investigation of the accuracy of high-order methods for hypersonic shock wave turbulent boundary layer interaction (SWTBLI) is presented. The numerical methods considered here comprise of the Monotone-Upstream Central Scheme for Conservation Laws (MUSCL) and Weighted Essentially Non-Oscillatory (WENO) schemes, $2^{nd}$ to $9^{th}$ order accurate in conjunction with structured and mixed element unstructured grids. Both Implicit Large Eddy Simulation (ILES) and Reynolds Averaged Navier-Stokes (RANS) computations have been performed. The effects of discretization on the turbulence transport equation, including the approximation method for the viscous gradient, are also investigated. The accuracy of the schemes in high Reynolds number RANS modeling is assessed against experimental data of a shock impingement on a flat plate at Mach number 5 and unit Reynolds number $37 \times 10^6$/m. ILES has been performed for the compression ramp case a moderate Reynolds numbers of $38.7 \times 10^3$, based on the boundary layer thickness, and compared to Direct Numerical Simulations (DNS).

**15. SUBJECT TERMS**

EOARD, Hypersonics, Turbulent Boundary Layer

| 16. SECURITY CLASSIFICATION OF: | | | 17. LIMITATION OF ABSTRACT | 18, NUMBER OF PAGES | 19a. NAME OF RESPONSIBLE PERSON |
|---|---|---|---|---|---|
| a. REPORT | b. ABSTRACT | c. THIS PAGE | | | Matt Snyder |
| UNCLAS | UNCLAS | UNCLAS | SAR | 20 | **19b. TELEPHONE NUMBER** *(Include area code)* +44 (0)1895 616420 |

**Standard Form 298** (Rev. 8/98)
Prescribed by ANSI Std. Z39-18

# Research Project

# Shock-Induced Turbulence and Acoustic Loading on Aerospace Structures

## First Year Report

### High-Order Methods for Supersonic and
### Hypersonic Shock Wave Turbulent Boundary Layer Interaction[1]

Dimitris Drikakis
University of Strathclyde,
Glasgow, UK
dimitris.drikakis@strath.ac.uk

An investigation of the accuracy of high-order methods for hypersonic shock wave turbulent boundary layer interaction (SWTBLI) is presented. The numerical methods considered here comprise of the Monotone-Upstream Central Scheme for Conservation Laws (MUSCL) and Weighted Essentially Non-Oscillatory (WENO) schemes, 2nd to 9th order accurate in conjunction with structured and mixed element unstructured grids. Both Implicit Large Eddy Simulation (ILES) and Reynolds Averaged Navier-Stokes (RANS) computations have been performed. The effects of discretization on the turbulence transport equation, including the approximation method for the viscous gradient, are also investigated. The accuracy of the schemes in high Reynolds number RANS modeling is assessed against experimental data of a shock impingement on a flat plate at Mach number 5 and unit Reynolds number $37 \times 10^6$/m. ILES has been performed for the compression ramp case at moderate Reynolds numbers of $38.7 \times 10^3$, based on the boundary layer thickness, and compared to Direct Numerical Simulations (DNS).

## I.  Introduction

S HOCK-WAVE turbulent boundary layer interaction (SWTBLI) is of particular interest to structural engineers for the design and manufacture of aerospace structures. Pulsating flows featuring unsteadiness attributed to SWTBLI can lead to fatigue and structural damages[1]. Advancing our understanding of SWTBLI and associated loading is important for developing effective control strategies that will mitigate these loads.

Numerical simulations of SWBLI flows are constrained by accuracy and computational cost. The accuracy is hampered by excessive numerical dissipation and dispersion errors. First and second order numerical schemes are highly dissipative, thus leading to incorrect predictions of turbulent SWTBLI induced separation. High-order (HO) schemes in conjunction with large eddy simulations lead to significantly better results, however, pressure fluctuations can be under-, or over-predicted, due to numerical dispersion errors. In the last few years, however, significant progress has been made with regards to the application of high-resolution (HR) and HO methods to compressible flows featuring acoustic excitation, turbulent SWTBLI, and low-Mach number effects.[2-6]

---

[1] The work presented in this report was carried out during the first year of the project, while the PI was at Cranfield University, Cranfield, MK43 0AL, UK

**The simulations and results presented in this report concern Cases 1 and 2 of the original program of work**, i.e. a shock of Mach number 5 (Re=37x10^{6}) impinging on a flat plate agitating the turbulent boundary layer and forming a separation zone; and implicit large eddy simulation of supersonic flow over a compression ramp. In the past, several efforts have been made to obtain reliable measurements for supersonic boundary layers[7]. The reported experimental results encompass an alarming degree of scatter for (nominally) compatible measurements performed in different facilities. Schülein[8] performed several experimental activities of SWTBLI flow at Mach 5. The state-of-the-art techniques were employed to measure wall pressure loadings, skin friction, velocity profiles and heat loads. This case has been extensively employed for validation and investigation of computational methods. The computed pressure loads are usually in good agreement with the experiment, however, considerable uncertainty is found in the skin friction predictions downstream of the boundary layer separation. In this paper, 2$^{nd}$ and 3$^{rd}$ order MUSCL, and 3$^{rd}$ and 5$^{th}$ order WENO numerical schemes, are employed to compute the supersonic turbulent flow at two shock-generator angles: 10 and 14 degrees. The RANS and ILES results are compared with experimental data[8] and DNS[35].

## II. Governing Equations

The governing equations are the 3D compressible Navier-Stokes equations, which can be written in the following Cartesian coordinates form after neglecting external body forces:

$$\frac{\partial}{\partial t} \iiint_V \vec{W}\, dV + \iint_A \left( \vec{F_c} - \vec{F_v} \right) dA = 0$$

$W$ is the vector of the conserved variables; and $F_c$ and $F_v$ are the inviscid and viscous fluxes, respectively:

$$\vec{W} = \begin{bmatrix} \rho \\ \rho u \\ \rho v \\ \rho w \\ \rho E \end{bmatrix}, \qquad \vec{F_c} = \begin{bmatrix} \rho \vee \\ \rho u \vee + n_x p \\ \rho v \vee + n_y p \\ \rho w \vee + n_z p \\ \rho E \vee \end{bmatrix}, \qquad \vec{F_v} = \begin{bmatrix} 0 \\ n_x \tau_{xx} + n_y \tau_{xy} + n_z \tau_{xz} \\ n_x \tau_{yx} + n_y \tau_{yy} + n_z \tau_{yz} \\ n_x \tau_{zx} + n_y \tau_{zy} + n_z \tau_{zz} \\ n_x \Theta_x + n_y \Theta_y + n_z \Theta_z \end{bmatrix}$$

where $\rho$ is the density, $u$, $v$ and $w$ are the velocity components, $p$ is the pressure and $E$ is the total energy per unit mass. The contravariant velocity is given by:

$$\vee = \vec{n} \cdot \vec{u} = n_x u + n_y v + n_z w$$

$$\Theta_x = u\tau_{xx} + v\tau_{xy} + w\tau_{xz} + k\frac{\partial T}{\partial x}$$

$$\Theta_y = u\tau_{yx} + v\tau_{yy} + w\tau_{yz} + k\frac{\partial T}{\partial y}$$

$$\Theta_z = u\tau_{zx} + v\tau_{zy} + w\tau_{zz} + k\frac{\partial T}{\partial z}.$$

where $\tau_{ij}$ are the shear stresses and $k$ is the heat conductivity constant. An ideal gas is assumed for the thermodynamic closure of the equations and the Sutherland's Law is used in the calculation of the dynamic viscosity.

# III. Numerical Methods

## A. Compressible unstructured grid framework

The equations are discretized by a k-exact Finite Volume (FV) method on mixed-element unstructured meshes. The MUSCL and WENO schemes are employed for reconstructing the element averaged solutions using high-order stencils and polynomial functions. A detailed description of the methods and their implementation can be found in[2,3]. A brief description of the methods is presented below.

The numerical approach adopted in the present study[25,26] is suitable for unstructured meshes with various types of element shapes in 2D and 3D. It has been previously used successfully for laminar, transitional and turbulent flows[2,27]. A Gaussian numerical quadrature of appropriate order for the order of the polynomial used is implemented for the approximation of the integral expressions of the fluxes. The calculation of the numerical convective and viscous fluxes requires the knowledge of the pointwise values of the conserved vector as well as of the velocity and temperature gradients at each Gaussian integration point. These pointwise values are approximated through an interpolation (reconstruction) procedure of a desired order of accuracy utilizing the cell averages. The latter requires a recursive stencil construction process where the direct side neighbor elements are added until a target number $M$ of stencil elements has been reached. For MUSCL-type schemes only one central stencil is used, while for WENO schemes, in addition to the central stencil, several additional directional stencils are also employed.

The reconstruction is carried out in a transformed system of coordinates in order to minimize scaling effects that appear in stencils consisting of elements of different sizes, as well as to improve the condition number of the system of equations[25,26]. For computing the degrees of freedom, a minimum of $K$ cells are needed in the stencil in addition to the target cell. Using the minimum possible number of cells in the stencil ($M \equiv K$) has been found to produce ill-conditioned systems[26,28-30], hence the choice to use $M = 2K$ improves the robustness of the method. This is especially worthwhile since no substantial performance penalty is incurred as a result of this improvement[26,30,31]. The resulting least-squares system is solved by a QR decomposition and the reconstruction polynomial is computed.

In the present study two different schemes are employed for discretizing the convective fluxes of the equations: a MUSCL scheme using a TVD-type slope limiter[32] and different WENO schemes[25,26] based on the characteristic variables. For the viscous part a linear reconstruction polynomial of the same order for the velocity and temperature field is constructed using the same central stencil as for the conserved vector. The discontinuous states of the convective fluxes are approximated by the HLLC Riemann solver[13], and the central averaging approach is used for the discontinuous viscous flux. The solution is advanced in time by an explicit TVD Runge-Kutta 3rd-order method[24]. It is worth mentioning that unstructured grids for complex geometries can benefit when combined with variational optimization techniques[33] as well as with very high order methods[34]. For RANS computations, the Spalart-Allmaras (SA)[11] one-equation turbulence model has been employed.

## B. Compressible structured-grid framework

The structured-grid code solves the full Navier-Stokes equations using a finite volume Godunov-type method. The inter-cell numerical fluxes are computed by solving the Riemann problem using the reconstructed values of the conservative variables at the cell interfaces. The reconstruction stencil is a one dimensional swept unidirectional stencil (1D split). The Riemann problem is solved using the Harten, Lax, van Leer, and (the missing) "Contact" (HLLC) approximate Riemann solver[13]. The reconstructed values utilized in the HLLC Riemann solver are obtained primarily by two different limiter approaches, the Monotone Upstream-centered Schemes for Conservation Laws[14] (MUSCL) and the Weighted-Essentially-Non-Oscillatory[15] (WENO) reconstruction methods. The MUSCL is employed with accuracy up to 5th order[16,17] (henceforth labeled M5), whereas the WENO schemes uses up to 9th-order of accuracy[18,19] (henceforth labeled W9). The 9th-order WENO is implemented in conjunction with a relative smoothness limiter[20] as well as a mapping technique[21].

All the reconstruction techniques can be further augmented with a low-Mach limiting scheme[5], which involves an additional stage in the reconstruction process for the velocity vector. This low-Mach number correction (labeled

as LM) ensures uniform dissipation of kinetic energy in the limit of zero Mach number, thus extending the validity of Godunov-type methods to at least Mach≈$10^{-4}$ via a progressive central differencing of the velocity components. It has been recently shown[22,23] that use of the low-Mach number correction can lead to a minor reduction in accuracy when used along with the 9th-order WENO. It was found that when the numerical dissipation is sufficiently small, dispersive errors originating from the WENO reconstruction can become dominant. Nonetheless, the 9th-order WENO was also shown to possess a remarkable inherent low-Mach number capability as it was able to successfully resolve flow features at relatively low Mach number regimes (Mach≈0.1) at moderate grid resolutions without the use of any low-Mach number correction method. In the light of the above, in the present study the low-Mach number correction method[5] was implemented only in conjunction with the 5th-order MUSCL scheme (henceforth labeled M5LM).

The viscous part of the equations is solved using a second order central difference scheme. Finally, the solution is advanced in time using a three-stage total variation diminishing (TVD) Runge-Kutta (RK) method[24].

## IV. Results

### A. Impinging shock

The case is based on the experiment of Schülein[8] where an incoming flow of Mach 5 and a unit Reynolds number of $37x10^6$/m is colliding with an inclined wall (shock generator), generating a shock that impinges on the bottom flat plate interacting with the flat plate boundary layer. The experimental set-up and the basic flow features in the vicinity of the SWBLI are shown in Figure 1.
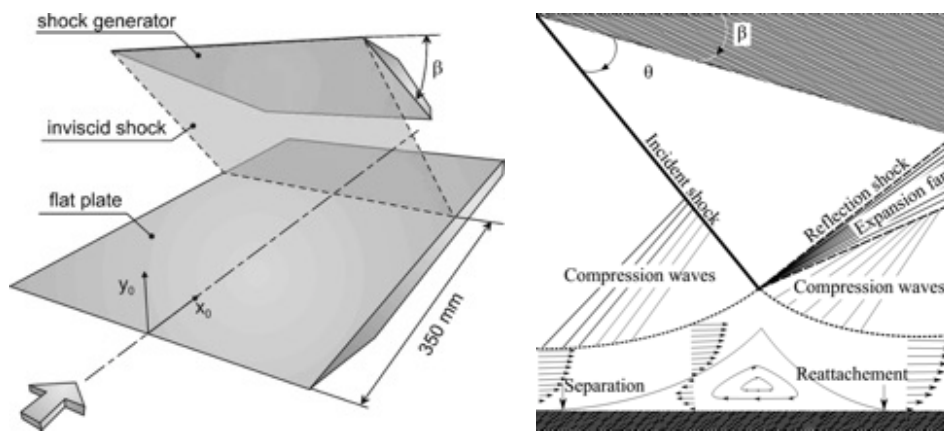


**Figure 1: Experimental set-up of Schülein (left) (adapted from Schülein[6]) and schematics of the flow physics near the SWTBLI region (right)**

The experimental data include wall pressure, skin friction coefficient and velocity profiles for three different shock generator angles: 6, 10 and 14 degrees. The cases for angles 10 and 14 degrees correspond to higher shock intensity levels compared with case 6, where the boundary layer is fully separated.
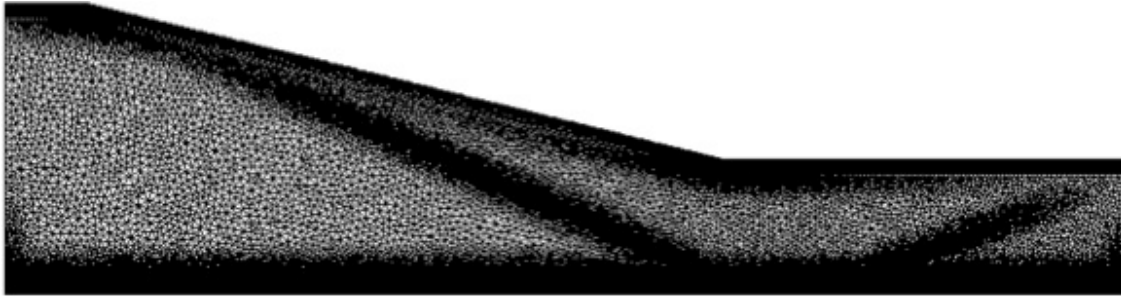
4

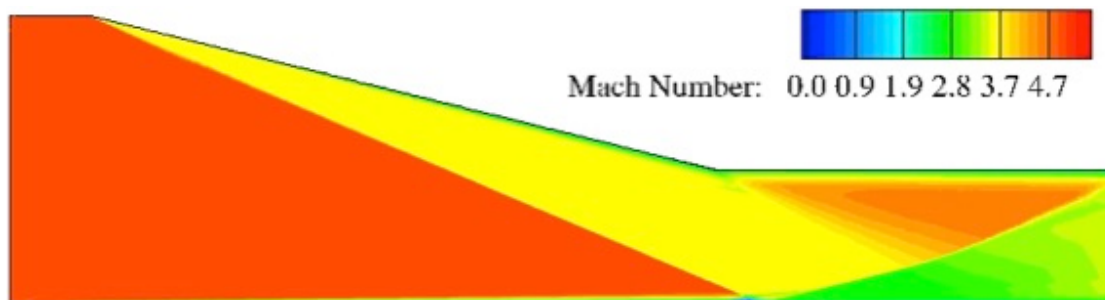**Figure 2: Fine grid at 14 degrees shock-generator angle for the SWTBLI.**



Mach Number: 0.0 0.9 1.9 2.8 3.7 4.7

**Figure 3: Mach number contours for the 14 degrees shock-generator angles results shown for the WENO 3$^{rd}$ order scheme.**

Computations were performed for shock-generator angles 10 and 14 degrees using the MUSCL and WENO schemes. The time integration was performed by a third-order explicit Runge-Kutta scheme. In the framework of RANS, a grid convergence study was performed using coarse, medium and fine grids consisting of 59,405, 96,879 and 179,997 elements, respectively. The grids are locally refined to capture the boundary layer effects and the impinging shock; Figure 2 illustrates the fine grid for case 14; the computed Mach number contour levels are shown in Figure 3 for the 3$^{rd}$-order WENO scheme.

The wall pressure and skin friction coefficient on the lower wall (flat plate) for the 2$^{nd}$-order MUSCL (M2) and 3$^{rd}$-order WENO (W3) schemes are compared with the experimental data for the 14 degrees case on the fine grid (Figure 4). Overall the agreement is acceptable for the pressure loads apart from the under-prediction near the separation point. In terms of skin-friction, considerable under-predictions are present downstream of the separation to the end of the flat plate. The W3 solution recovers better featuring smaller oscillations in the recirculation region ($300 < x < 350$).

Two different techniques were employed for the discretization of the turbulence transport equation: i) using the same reconstruction as for the mean flow equations[4] (labeled as coupled approach); ii) using a first order upwind method (labeled as decoupled approach). The results are shown in Figure 5, where the coefficient of skin friction is plotted for the 10-degree case on the medium grid.[12] Furthermore, the viscous gradient computation method has been investigated in conjunction with the Green Gauss (GG) and the least-square method (LSQ). It was found that the profile obtained by the LSQ method provides better agreement with the experiment near the recirculation region. The Mach number boundary layer profile is plotted for the 10 degrees case at two stations in Figure 6 showing satisfactory agreement with the experiment.
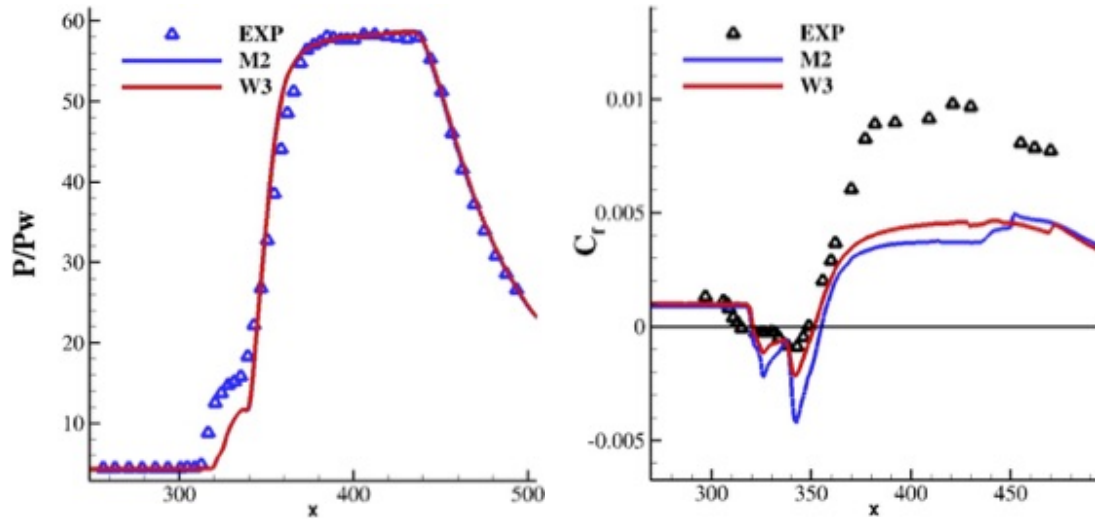
**Figure 4: Dimensionless wall pressure on the lower wall (left) and skin friction coefficient (right). The computations using the MUSCL 2$^{nd}$-order (M2) and WENO 3$^{rd}$-order (W3) schemes are compared with the experiment.**
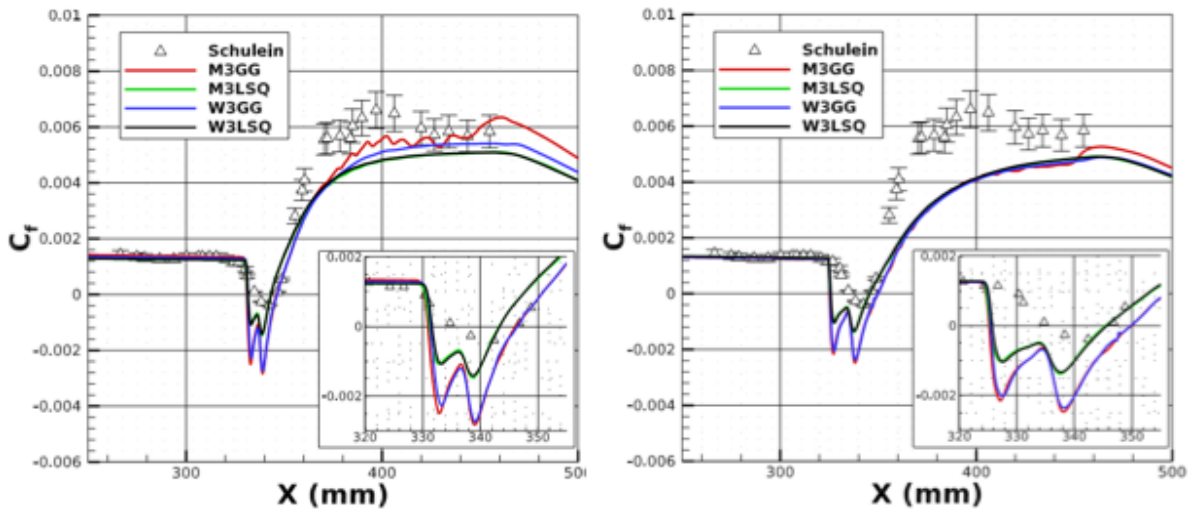


**Figure 5: Skin friction coefficient on the lower wall for the 10 degrees case, for the M3 and W3 schemes with two different viscous gradient methods, the Green Gauss (GG) and the Least Square method (LSQ); coupled results are shown on the left and decoupled results are shown on the right.**
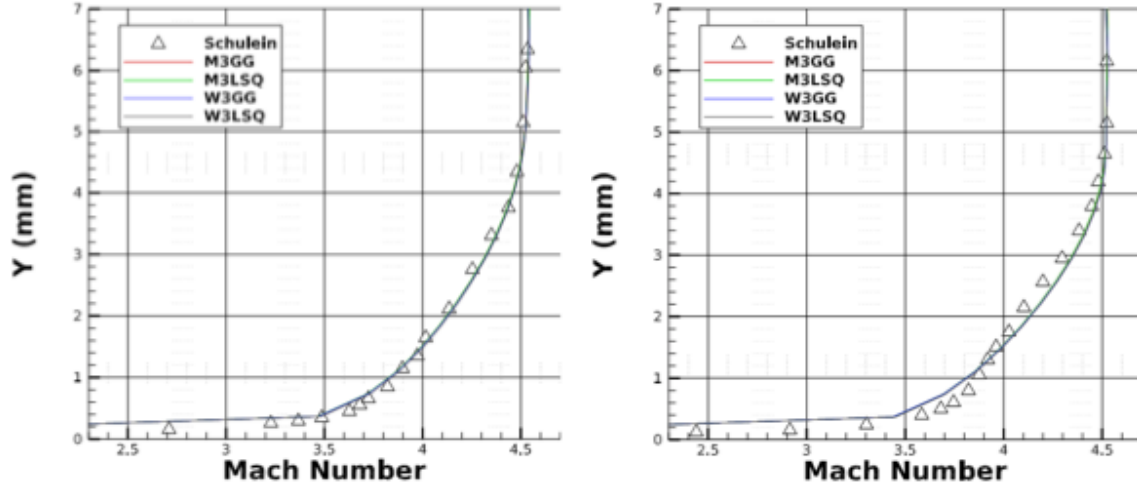
6

**Figure 6: Mach number profiles for the 10 degrees case at two different stations; left at x=396mm and right at x=426mm.**

## B. Compression ramp

ILES has been performed to simulate the shock wave/turbulent boundary layer interaction (SWTBLI) over a compression ramp. The structured finite volume code CNS3D will be used, which numerical background is given in section §III B. The case is based on the DNS study of Wu and Martin[35] where an incoming flow of Mach 2.9 and a Reynolds number of $38.7 \times 10^3$ based on the freestream properties and boundary layer height ($\delta$) collides with a surface as the wall in inclined abruptly by 24°, generating a shock that interacts with the incoming turbulent flow. The boundary layer forms a separation bubble with its size being dictated by the intensity of the incoming turbulent flow and the strength of the formed shockwave.

The effects of grid resolution was investigated using three different grids (see Table 1). Each level of grid refinement used a smaller y+ value of the first point from the wall. Previous investigations[22] regarding low-Mach compressible turbulent boundary layers, have shown that y+ values of around 2 is sufficient, at least for the 9th-order WENO scheme. Furthermore, the 5th-order MUSCL in conjunction with the low-Mach number correction of[5] is expected to provide accurate results. The low-Mach correction is required for capturing the subsonic region of the incoming turbulent boundary layer and its influence decreases linearly to zero as the transonic boundary limit is reached.

|         | Nx   | Nz  | Ny  | z+  |
|---------|------|-----|-----|-----|
| **Coarse**  | 600  | 96  | 72  | 2   |
| **Medium**  | 840  | 120 | 96  | 1   |
| **Fine**    | 1128 | 168 | 120 | 0.5 |
| **DNS**[35] | 1024 | 160 | 128 | 0.2 |

**Table 1: Grid resolution in number of cells**

The size of the computational domain used is compared to that of the DNS in Table 2. Note that the height of the domain at the inflow location has remained the same. However a larger streamwise length was utilized in order to accommodate the spatially developing turbulent boundary layer.

7

| | $L_x$ | $L_y$ | $L_z$ |
|---|---|---|---|
| **ILES** | 21.4 | 3 | 5 |
| **DNS**[35] | 15.4 | 2.2 | 5 |

**Table 2: Size of computational domain (in terms of $\delta$).**

Periodic boundary conditions were used in the spanwise (y) direction. In the wall-normal (z) direction, a no-slip isothermal wall ($T_W$=309K) was used. Supersonic outflow was prescribed at the outlet, while free stream conditions (far-field) were assigned at the upper boundary opposite to the wall. The boundary condition at the inlet requires of accurately assigning a turbulent boundary layer. A synthetic turbulent digital filter approach[36] was further developed in conjunction with the present numerical framework[37] to generate incoming turbulent boundary layer data. It is shown to work satisfactorily and has since been used successfully in a number of different test-cases[38,39,40]. Note that since the numerical scheme still needs to capture and resolve the synthetic inflow perturbations that lead to a turbulent flow, the length of the upstream domain is increased by approximately five boundary layer heights.
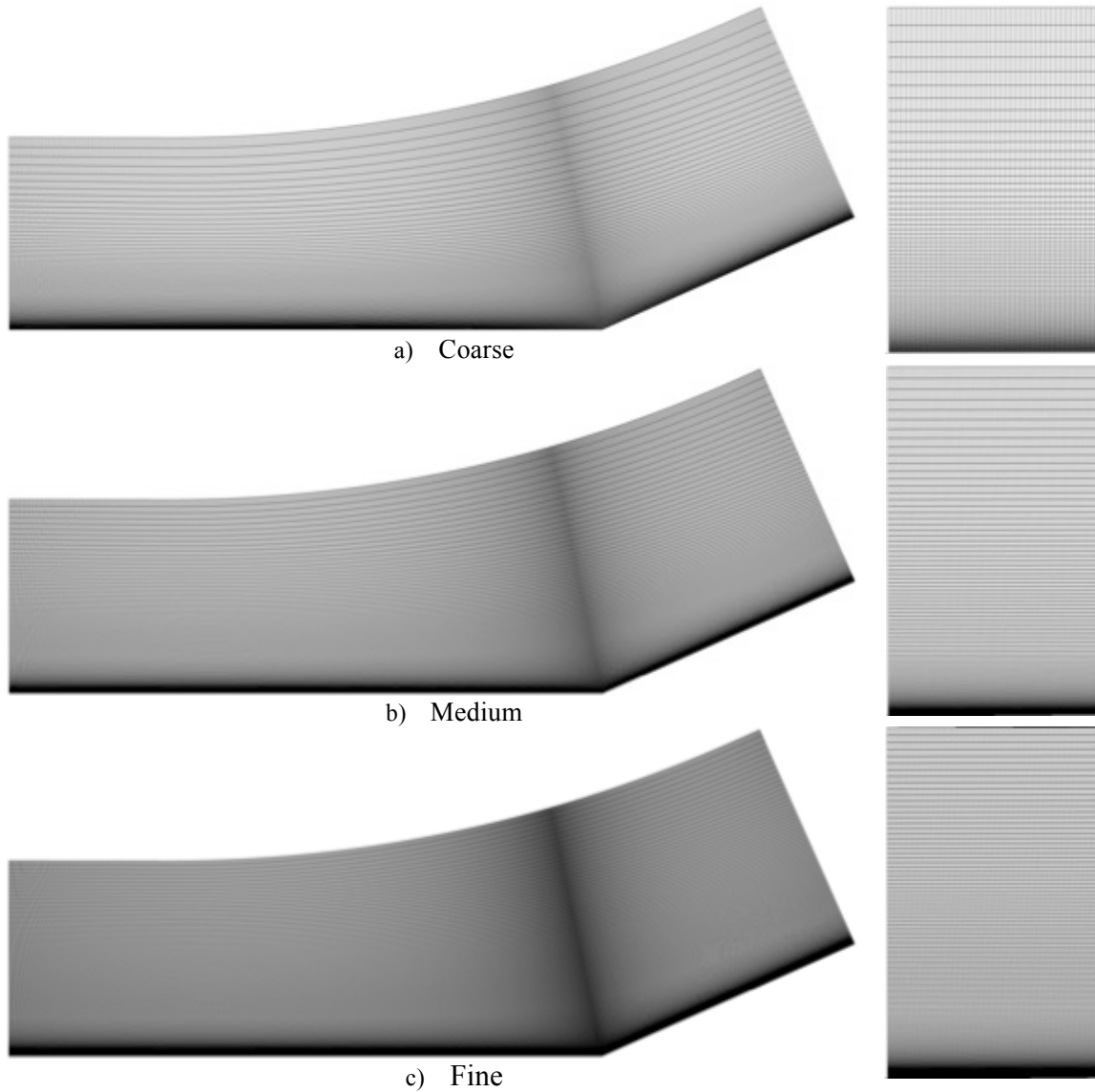


a)   Coarse

b)   Medium

c)   Fine

**Figure 7: Computational grids for the ramp case.**

The computational grids are shown in Figure 7. The coarse grid comprises 4,147,200 cells, while the medium and fine grids comprise of 9,676,800 and 22,740,480, respectively.

In order to reduce the computational cost, particularly on the fine grid, a variable limiter approach was employed. The 9th-order WENO is more expensive than the 2nd and 5th-order schemes due to the increased number of candidate stencils. Using a reduced order of accuracy in the outer region of the supersonic laminar flow does not negatively impact on the accuracy of the results in the near wall region. Any disturbances that arise from the inner turbulent boundary layer are steadily advected, but more rapidly dissipated. A 2nd-order MUSCL limiter is used (Monotonized Central, MC) in the outer wall regions of the flow allowing for the more computationally expensive 5th-order MUSCL and 9th-order WENO schemes to be used in the near wall region. The computational cells located further than two boundary layer thicknesses ($2\delta$) from the closest wall point are deemed marginal and assigned to the lower numerical accuracy region. **Error! Reference source not found.** shows the resulting regions of low and high-order of accuracy as applied to the compression ramp geometry and settings described.
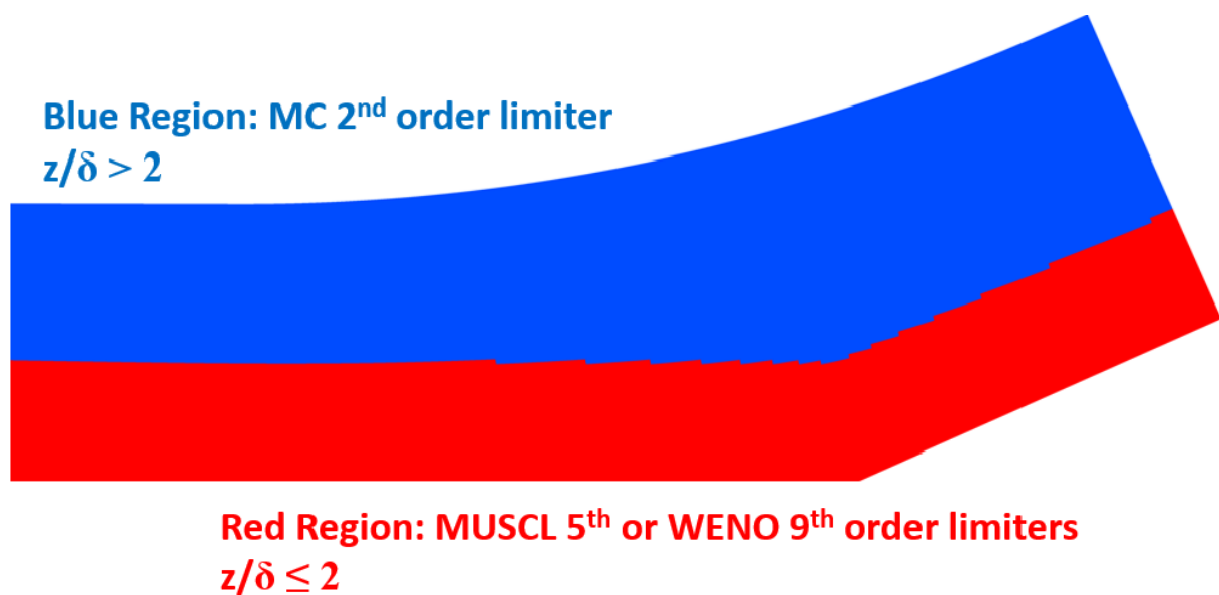


**Blue Region: MC 2nd order limiter**
**$z/\delta > 2$**

**Red Region: MUSCL 5th or WENO 9th order limiters**
**$z/\delta \leq 2$**

**Figure 8: Variable limiter regions**

The reduction of computational cost gained by implementing variable limiter regions depends on the block partitioning of the domain conducted for parallel processing. In the case of the 9th-order WENO the variable limiter region approach was found to speed up the computations by approximately 10-20%.

As remarked earlier, the size of the separation bubble will highly depend on the nature of the turbulent flow resolved. This is because the turbulent boundary layer will frequently deposit large amounts of momentum near the wall surface, which acts to push the "growing" separation bubble back. In the presence of a laminar boundary layer, a separation bubble is expected to gradually increase in size by gradually "creeping" upstream via the subsonic part of the boundary layer. Turbulence acts to impede on this process by moving supersonic flow of high momentum and kinetic energy closer to the wall surface.

Figure 9 gives a qualitative comparison of the level of turbulence resolved by each numerical method and grid resolution examined by plotting the iso-surfaces of the Q-criterion. As expected, each level of grid refinement leads to an increase in the amount and strength of vortex cores resolved. Noticeably, the 9th-order WENO on the coarse grid appears capable of resolving a similar number of vortices in the region preceding the separation bubble as the 5th-order MUSCL. An integral length scale of $2\Delta x$ in the streamwise direction was chosen for the digital filter turbulent inflow technique. Past the shockwave front, the grid refinement appears to have little to no effect on the structure of the vortices resolved by the 9th-order WENO. On the contrary, the 5th-order MUSCL shows a gradual improvement in the resolved turbulent structure, which eventually resembles that obtained by the 9th-order WENO.
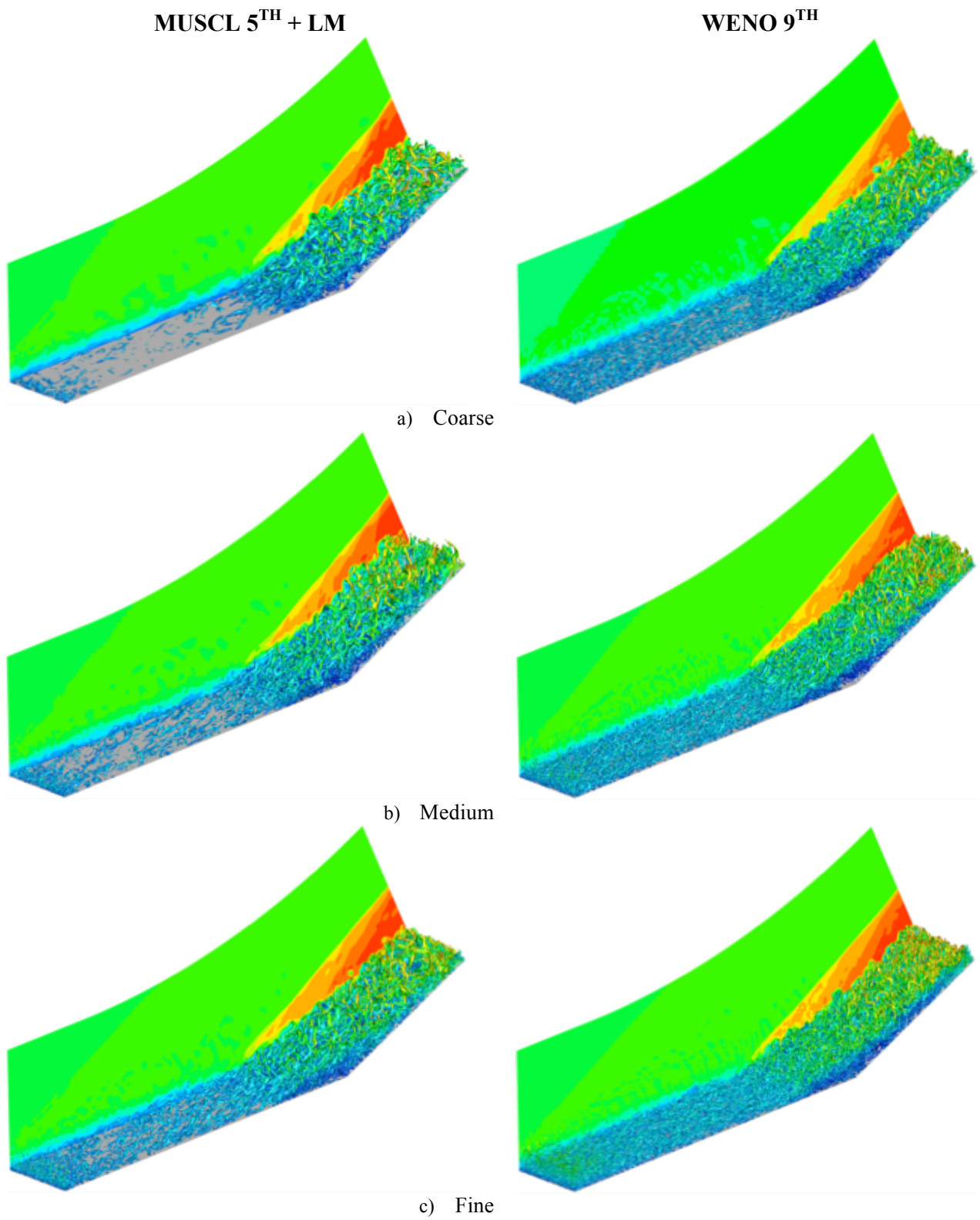
9

MUSCL 5TH + LM          WENO 9TH



a) Coarse

b) Medium

c) Fine

**Figure 9: Iso-surfaces of *Q*-criterion; $Q \cdot (\delta/U_\infty)^2 = 2$ & 5 colored by $\rho/\rho_\infty \in [-0.2, 2]$ as xz-plane contour plot.**

10

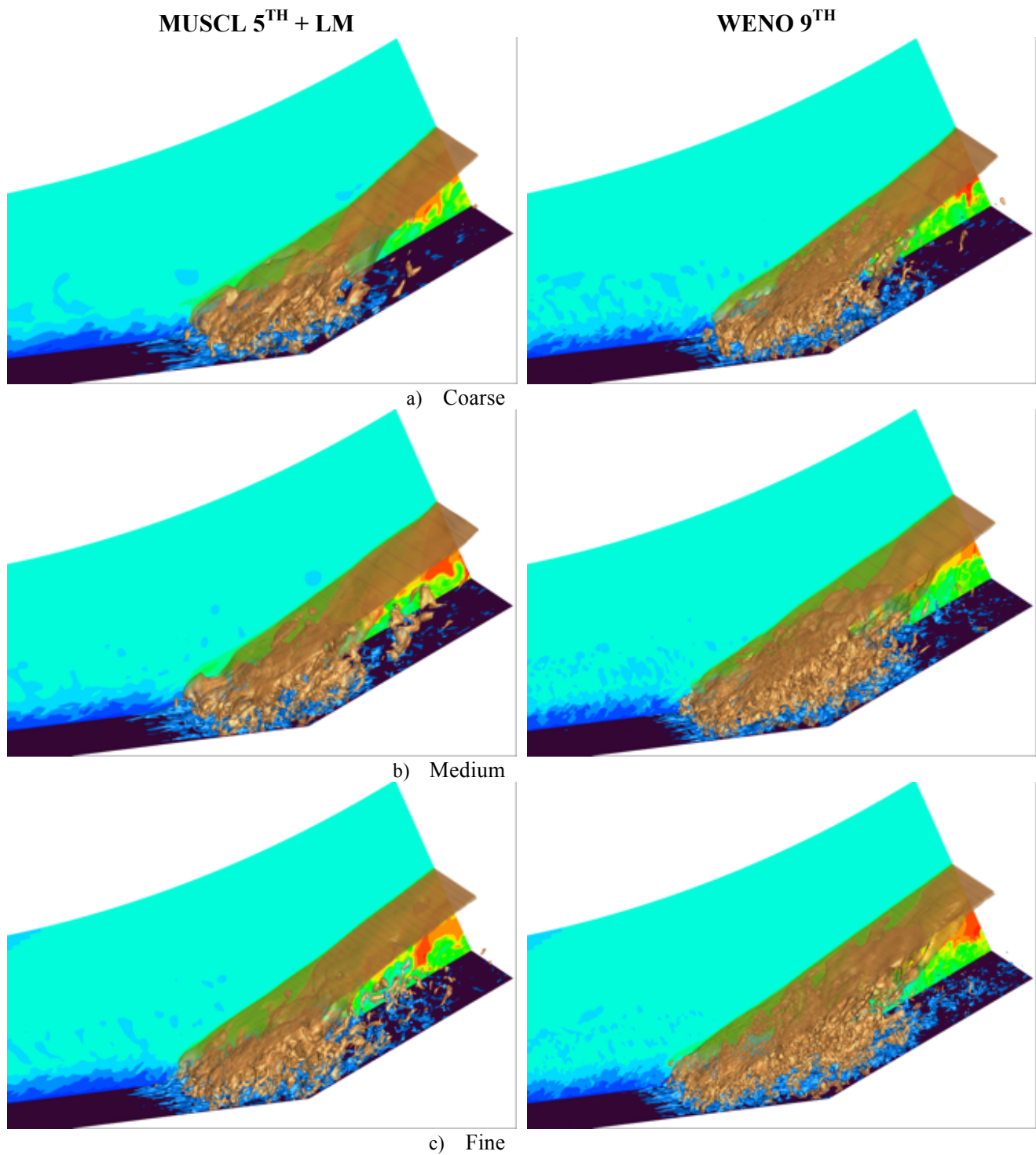**MUSCL 5$^{TH}$ + LM**  **WENO 9$^{TH}$**



a) Coarse

b) Medium

c) Fine

**Figure 10: Iso-surfaces depicting shock-bubble interaction; blue: separation bubble $\rho u=0$, orange: shock pressure $P/P_w \approx 1.765$ & $2.353$, xz-plane: contrours of $\rho/\rho_\infty \epsilon [0.4,3]$.**

11

Figure 10 illustrates the interaction of the separation bubble and shockwave. The most important factor that determines the physical processes occurring here is the incoming turbulent flow, which relies largely on the numerical scheme used as already discussed. The "streaky" appearance of the separation bubble's leading edge is a result of the incoming turbulent flow, which deposits energy from the freestream onto the near-wall surface. The effect is to push random areas of the bubble downstream, thus causing the observed streaks. The shockwave pressure front is found to be more unsteady-like (as evident by the wavy-like structure) in the frontal region of the separation bubble. However this becomes less evident as the grid is refined. The cause for this unexpected result is the turbulent integral length scales produced by the turbulent inflow digital filter technique, which relies on the inflow cell length to give a value to the streamwise turbulent integral length scale. Increasing the number of computational cells leads to estimating smaller turbulent integral length scales fed into the digital filter. This leads inevitably to smaller "large" turbulent integral scales produced in the flow, which cannot "carry" as much energy from the freestream to the near-wall region, thus greatly affecting the strong shockwave pressure front formed.
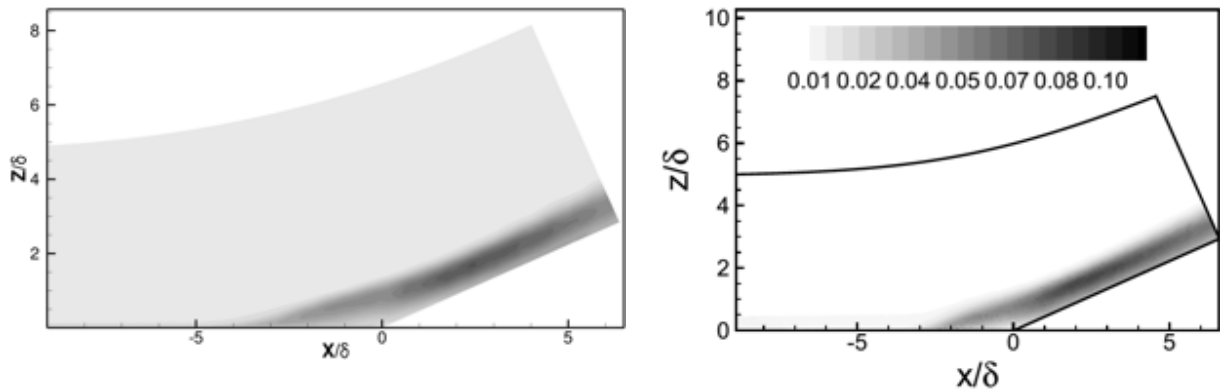


**Figure 11: Contours of time-averaged TKE $\overline{\rho u' u'} / 2\rho_\infty U_\infty^2$ ; (left: ILES coarse grid W9, right: DNS[35]).**

The time-averaged turbulent kinetic energy (TKE) resolved by the 9th-order WENO scheme on the coarse grid, as seen in Figure 11, is consistent to that obtained by the DNS of Wu and Martin[35], albeit the maximum TKE is found over a lesser area. Nevertheless, this is still a very encouraging result considering the difference in the total number of cells used in either case.
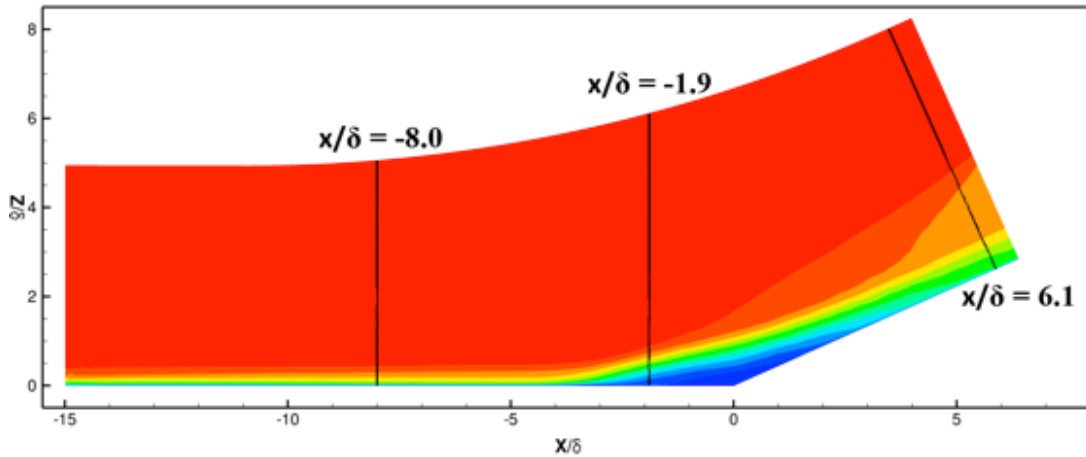


**Figure 12: Location of velocity profiles used for comparisons with DNS.**

12

Figure 12 shows the locations along which time-averaged velocity profiles are compared to DNS. Three locations are chosen: i) the first is located in the incoming turbulent inflow and acts as a good measure of the quality of the resolved mean turbulent profile; ii) the next is located prior to the compression corner but within the leading front of the separation bubble and acts as an indicator of how well the separation bubble is captured; and, finally, iii) the last is located just prior to the domain exit (outflow boundary condition) and reveals whether the correct turbulent profile and shock position are captured.

The mean turbulent velocity profiles (Figure 13) show a satisfactory agreement to DNS. Generally, the 9th-order WENO captures a sharper velocity gradient in the near-wall region than the 5th-order MUSCL scheme. Most interestingly, however, the 9th-order WENO results obtained on the coarse grid agree best to the DNS. This is due to the dependence of the turbulent integral length scale used by the digital filter on the grid resolution, as previously explained.
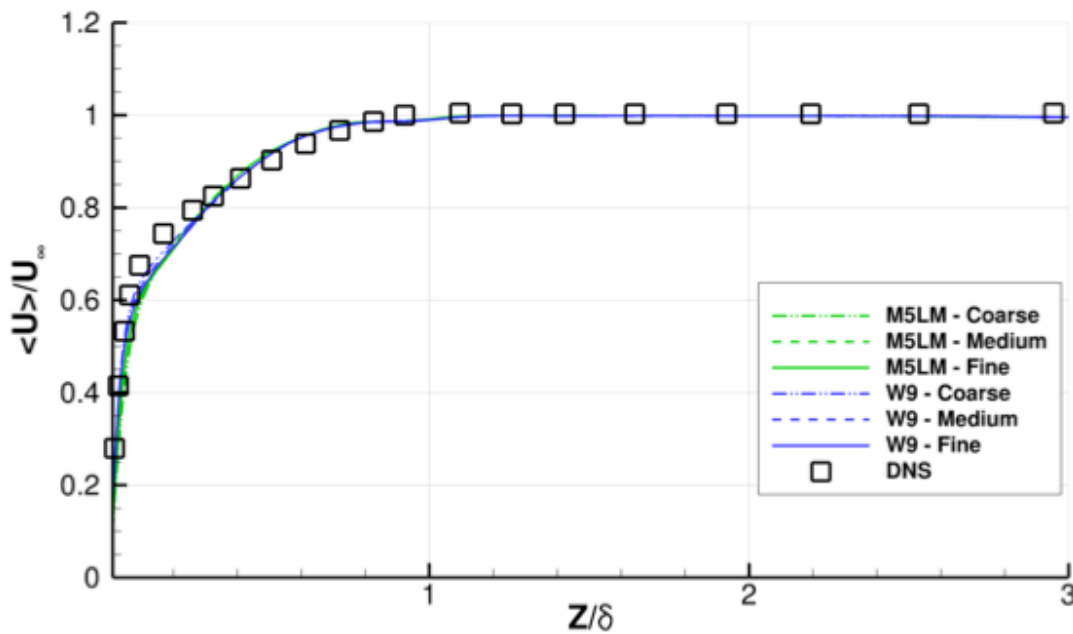


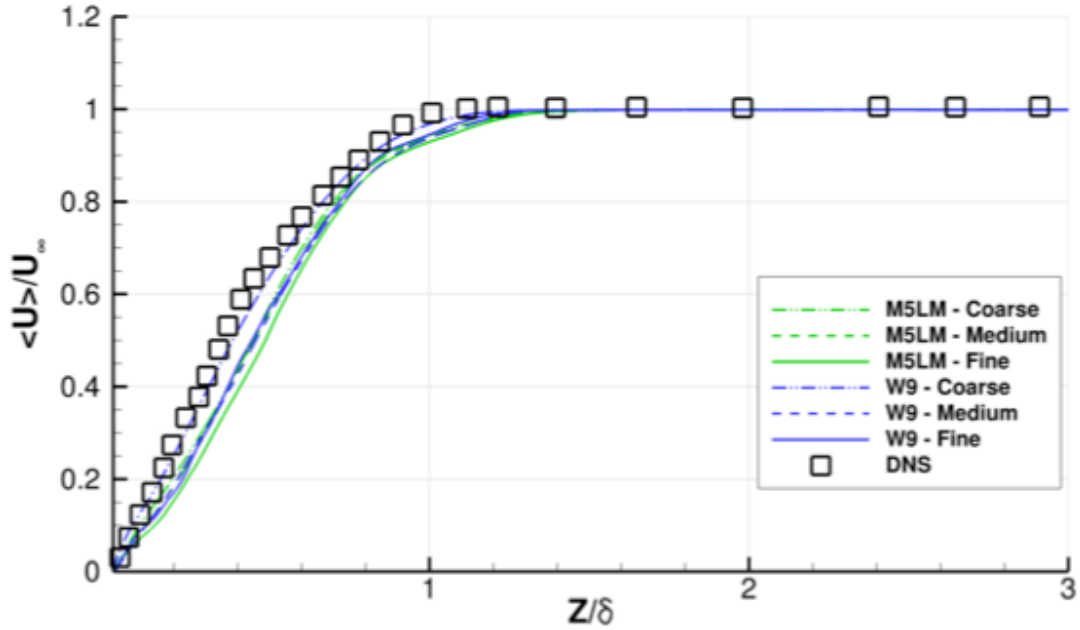**Figure 13: Velocity profile comparisons at $x/\delta_0 = -8$.**

**Figure 14: Velocity profile comparison at $x/\delta_0$=-1.9.**

The impact on the results of the decreasing turbulent length scales associated with the increased grid resolution becomes more evident in Figure 14. The 5th-order MUSCL seems to be less sensitive to the grid resolution, however, this is partly due to its reduced ability to resolve features of two cell lengths imposed at the inflow by the digital filter. In the post-shock region and just prior to the outflow, Figure 15 shows that the 5th-order MUSCL scheme has given a better agreement to the DNS than the 9th-order WENO. It is difficult to ascertain a reason for this occurrence at this early stage, but the erroneous results obtained upstream could be partly to blame. On another note, the transition from the high-order to the low-order region does not appear to produce any kind of unphysical behavior at least to the mean velocity profile examined in Figure 15.
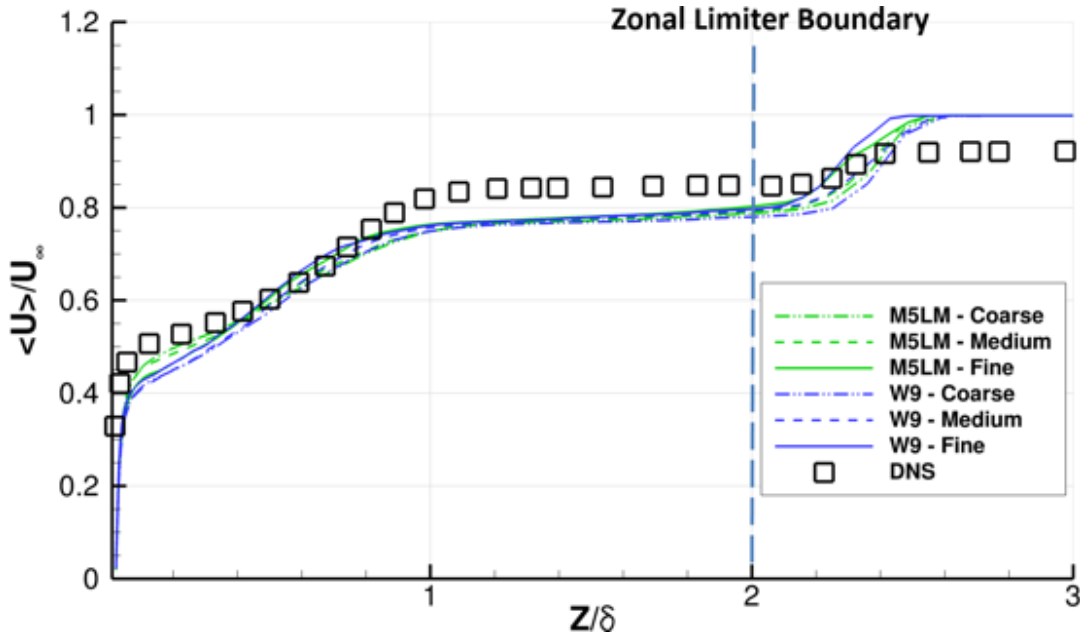


**Figure 15: Velocity profile comparison at $x/\delta_0$=-6.1.**

14

The mean wall pressure distribution obtained by the 5th-order MUSCL with low-Mach correction and the 9th-order WENO are compared to DNS[35] and experiment[41] in Figures 17 and 18, respectively. Both schemes give the best agreement on the coarse grid, as evident by the pressure profile at the separation bubble that begins at $x/\delta$=-5 up to the corner at $x/\delta$ =0. In the remaining regions, both schemes on all grids give wall pressure values that fall within those obtained by DNS and experiment.
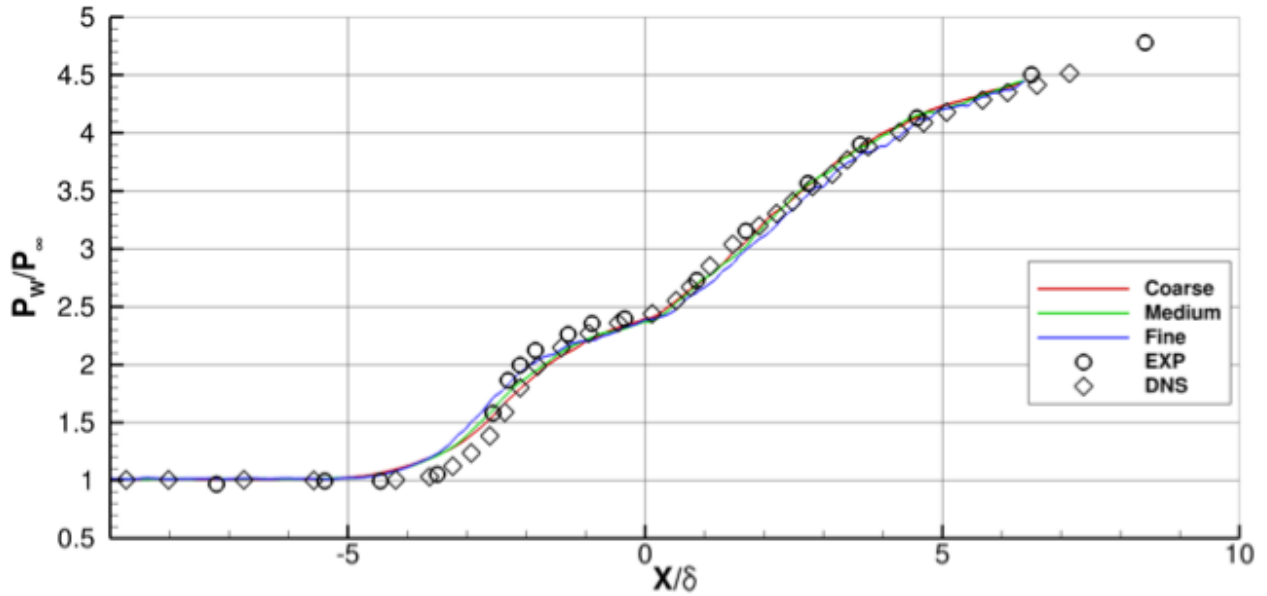


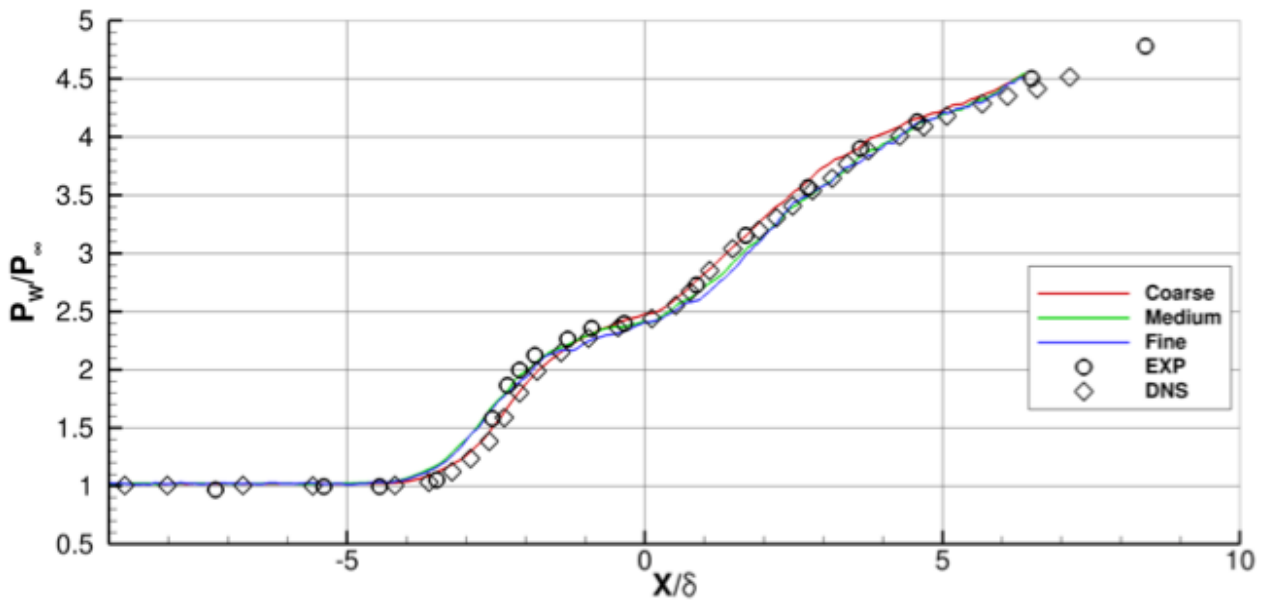**Figure 16: Mean wall pressure distribution for M5LM.**



**Figure 17: Mean wall pressure distribution for W9.**

# V. Conclusions

The capability of high-order, high-resolution methods is examined in the context of shock wave/turbulent boundary layer interaction (SWTBLI) from moderate to high Reynolds numbers. An unstructured solver was used to model an impinging shock at a sufficiently high Reynolds numbers that required application of the Spalart-Allmaras (SA)[11] turbulence model. Overall results are found to be encouraging, albeit a number of issues regarding numerical stability of the simulations required investigation. Agreement of the pressure loads is found to be acceptable apart from the under-prediction near the separation point. In terms of skin-friction considerable under-predictions are present downstream of the separation to the end of the flat plate. The 3$^{rd}$-order WENO solution recovered better featuring smaller oscillations in the recirculation region (300<x<350). It is also found that the profile obtained by the least-square method (LSQ) provides better agreement with the experiment near the recirculation region. The Mach number boundary layer profile also showed satisfactory agreement with the experiment. With regards to the turbulence model, coupling it to the same numerical schemes used during the estimation of the inviscid fluxes, namely the reconstruction method, resulted in superior accuracy compare to the traditionally used 2$^{nd}$-order central method.

The accuracy of the 5$^{th}$-order MUSCL, in conjunction with the low-Mach correction, and the 9$^{th}$-order WENO schemes were investigated in SWTBLI over a compression ramp. The Reynolds number was sufficiently low to allow for ILES to be conducted. The results showed a great deal of sensitivity to the resolved incoming turbulent flow produced using the digital filter technique. Time-averaged streamwise velocity and wall pressure profiles suggest that the finer (smaller) largest integral scales produced by the digital filter, as a result of the dependence of the estimation of the turbulent length scales to the inflow cell size, produces a "weaker" structure that can move less kinetic energy from the freestream to the inner-wall regions of the boundary layer. As a result, increasing the grid resolution causes the leading edge of the separation bubble to move un-physically further upstream. The 5$^{th}$-order MUSCL was not accurate enough to sufficiently resolve the perturbations produced by the digital filter based on mean turbulent integral scales of twice the cell length. Finally, a variable limiter region approach was implemented that reduced the computational requirements by 10% to 20% depending on the numerical scheme and a careful (MPI) block decomposition.

# References

[1]Pozefsky, P., Blevins, R.D and Laganelli, A.L., "Thermo-Vibro-Acoustic Loads and Fatigue of Hypersonic Flight Vehicle Structure", *AFWAL-TR-89-3014,* Feb. 1989.

[2]Tsoutsanis, P., Antoniadis, A.F., Drikakis, D., "WENO schemes on arbitrary unstructured meshes for laminar, transitional and turbulent flows", *Journal of Computational Physics*, 256 (2014) 254-276.

[3]Antoniadis, A.F., Tsoutsanis, P., and Drikakis, D., "Numerical accuracy in RANS computations of high-lift multi-element airfoil and aircraft configurations" *AIAA SciTech*, 53rd Aerospace Sciences Meeting, 2015.

[4]Antoniadis, A.F., Tsoutsanis, P., Rana, Z., Kokkinakis, I., and Drikakis, D., "Azure: an advanced CFD software suite based on high-resolution and high-order methods" *AIAA SciTech*, 53rd Aerospace Sciences Meeting, 2015.

[5]Thornber, B., Mosedale, A., Drikakis, D., Youngs, D., Williams, R.J.R, "An Improved Reconstruction Method for Compressible Flows with Low Mach Number Features", *Journal of Computational Physics*, 227 (2008) 4873-4894.

[6]Thornber, B., and Drikakis, D., "Implicit Large Eddy Simulation of a Deep Cavity Using High-Resolution Methods", *AIAA Journal,* Vol. 46, No. 10, 2634-2685, October 2008.

[7]Beresh, S.J., Henfling, J.F., Spillers, R.W., and Pruett, B.O.M., "Measurement of Fluctuating Wall Pressures Beneath a Supersonic Turbulent Boundary Layer", *AIAA Journal*, 2010-305, 2010.

[8]Schülein, E., "Skin-friction and heat flux measurements in shock/boundary-layer interaction flows", *AIAA J. 44 (8)* (2006) 1732–1741.

[9]Leger, T., and Poggie, J.," Computational analysis of shock wave turbulent boundary layer interaction", *AIAA SciTech,* 52nd Aerospace Sciences Meeting, AIAA 2014-0951, Jan.

[10]Fedorova, N. N., and Fedorchenko, I. A., "Computation of Interaction of an Incident Oblique Shock Wave with a Turbulent Boundary Layer on a Flat Plate," *Journal of Applied Mechanics and Technical Physics*, Vol. 45, No. 3, 2004.

[11]Spalart, P.R., Allmaras, S.R. One-equation turbulence model for aerodynamic flows, *Rech. Aérosp.* 1 (1994) 5–21.

[12]Smith I. "Investigation of High-Order schemes on unstructured grids for shock-wave turbulent boundary layer interaction flows", *MSc Thesis,* Cranfield University, 2013.

[13]Toro, E. F. "Riemann solvers and numerical methods for fluid dynamics: a practical introduction", 2009.

[14]Leer, B. van, "Towards the ultimate conservative difference scheme. II. Monotonicity and conservation combined in a second-order scheme, *Journal of Computational Physics,* 14 (4) (1974) 361–370.

[15]Liu, X.-D., Osher, S., Chan, T., "Weighted essentially Non-oscillatory schemes", *Journal of Computational Physics,* 115 (1) (1994) 200-212.

[16]Kim, K.H., Kim, C., "Accurate, efficient and monotonic numerical methods for multi-dimensional compressible flows: Part I: Spatial discretization", *Journal of Computational Physics,* 208 (2) (2005) 527–569.

Kim, K.H., Kim, C., "Accurate, efficient and monotonic numerical methods for multi-dimensional compressible flows: Part II: Multidimensional limiting process", *Journal of Computational Physics,* 208 (2) (2005) 570–615.

[18]Jiang, G.-S., Shu, C.-W., "Efficient implementation of weighted ENO schemes", *Journal of Computational Physics,* 126 (1) (1996) 202–228.

[19]Balsara, D.S., Shu, C.-W., "Monotonicity preserving weighted essentially non-oscillatory schemes with increasingly high order of accuracy", *Journal of Computational Physics*, 160 (2) (2000) 405–452.

[20]Taylor, E.M., Wu, M., Martin, M.P., "Optimization of nonlinear error for weighted essentially non-oscillatory methods in direct numerical simulations of compressible turbulence", *Journal of Computational Physics*, 223 (1) (2007) 384–397.

[21]Henrick, A. K., Aslam, T. D. and Powers, J. M., "Mapped Weighted Essentially Non-oscillatory Schemes: achieving optimal order near critical points", *Journal of Computational Physics*, 207 (2005) 542-567.

[22]Kokkinakis, I.W., Drikakis, D., "Implicit Large Eddy Simulation of weakly-compressible turbulent channel flow", *Computer Methods in Applied Mechanics and Engineering*, 287 (2015) 229-26.

[23]Tsoutsanis, P., Kokkinakis, I.W., Könözsy, L., Drikakis, D., Williams, R.J.R., Youngs, D.L., "Comparison of structured- and unstructured-grid, compressible and incompressible methods using the vortex pairing problem", *Computer Methods in Applied Mechanics and Engineering*, 293 (2015) 207-231.

[24]Shu, C.-W., Osher, S., "Efficient implementation of essentially non-oscillatory Shock-Capturing schemes", *Journal of Computational Physics*, 77 (2) (1988) 439–471.

[25]Titarev, V., Tsoutsanis, P., Drikakis, D., "WENO schemes for mixed-element unstructured meshes", *Communications in Computational Physics*, 8 (3) (2010) 585-609.

[26]Tsoutsanis, P., Titarev, V., Drikakis, D., "WENO schemes on arbitrary mixed-element unstructured meshes in three space dimensions", *Journal of Computational Physics,* 230 (4) (2011) 1585-1601.

[27]Antoniadis, A., Tsoutsanis, P., Drikakis, D., "High-order schemes on mixed-element unstructured grids for aerodynamic flows", *42nd AIAA Fluid Dynamics Conference and Exhibit* (2012).

[28]Haselbacher, A., "A WENO reconstruction algorithm for unstructured grids based on explicit stencil construction", *43rd AIAA Aerospace Sciences Meeting and Exhibit* - Meeting Papers (2005) 3369-3378.

[29]Hu, G., Li, R., Tang, T., "A robust WENO type finite volume solver for steady Euler equations on unstructured grids", *Communications in Computational Physics*, 9 (3) (2011) 627-648.

[30]Dumbser, M., Kaser, M., "Arbitrary high order non-oscillatory finite volume schemes on unstructured meshes for linear hyperbolic systems", *Journal of Computational Physics*, 221 (2) (2007) 693-723.

[31]Dumbser, M., Boscheri, W., "High-order unstructured Lagrangian one-step WENO finite volume schemes for non-conservative hyperbolic systems: Applications to compressible multi-phase flows", *Computers & Fluids*, 86 (2013) 405-432.

[32]Barth, T., Jespersen, D., "The design and application of upwind schemes on unstructured meshes", in: 27th AIAA Aerospace Sciences Meeting and Exhibit.

[33]Garanzha, V., Kudryavtseva, L., Utyuzhnikov, S., "Variational method for untangling and optimization of spatial meshes", *Journal of Computational and Applied Mathematics*, 269 (2014) 24-41.

[34]Titarev, V., Toro, E., "ADER: arbitrary high order Godunov approach", *Journal of Scientific Computing*, 17 (1-4) (2002) 609-618.

[35]Wu, M., Martin, M.P., "Direct Numerical Simulation of Supersonic Turbulent Boundary Layer over a Compression Ramp", *AIAA Journal*, 45 (4) (2007) 879-889.

[36]Rana, Z.A., Thornber, B.J.R., Drikakis, D., "Simulations of the HyShot-II (scramjet) model using high-resolution methods", 45th AIAA/ASME/SAE/ASEE Joint Propulsion Conference and Exhibit (2009).

17

[37]Rana, Z.A., Drikakis, D., Thornber, B.J. "Investigation of sonic jet mixing in a stream of supersonic cross-flow using large eddy simulations", 27th Congress of the International Council of the Aeronautical Sciences, ICAS 2010 (4) 2801-2813.

[38]Rana, Z.A., Thornber, B., Drikakis, D., "Transverse jet injection into a supersonic turbulent cross-flow", *Physics of Fluids*, 23 (4) (2011)

[39]Rana, Z.A., Thornber, B., Drikakis, D., "On the importance of generating accurate turbulent boundary condition for unsteady simulations", *Journal of Turbulence*, 12 N35 (2011) 1-39.

[40]Touber, E., Sandham, N.D., "Large-eddy simulation of low-frequency unsteadiness in a turbulent shock-induced separation bubble", *Theoretical and Computational Fluid Dynamics*, 23 (2) (2009) 79-107.

[41]Bookey, P. B., Wyckham, C., Smits, A. J., and Martin, M. P., "New Experimental Data of STBLI at DNS/LES Accessible Reynolds Numbers," *AIAA*, Paper No. 2005-309, Jan. (2005)